Article

Comparison and Evolution of Extreme Rainfall-Induced Landslides in Taiwan

Chunhung WU

Department of Water Resources Engineering and Conservation, Feng Chia University, No. 100, Wenhua Rd., Xitun District, Taichung City 407, Taiwan; chhuwu@fcu.edu.tw; Tel.: +886-4-2451-7250 (ext. 3223); Fax: +886-4-2451-5827

Abstract: This study analyzed the characteristics of, and locations prone to, extreme rainfall-induced landslides in three watersheds in Taiwan, as well as the long-term evolution of landslides in the Laonong River watershed (LRW), based on multiannual landslide inventories during 2003–2014. Extreme rainfall-induced landslides were centralized beside sinuous or meandering reaches, especially those with large sediment deposition. Landslide-prone strata during extreme rainfall events were sandstone and siltstone. Large-scale landslides were likely to occur when the maximum 6-h accumulated rainfall exceeded 420 mm. All of the large-scale landslides induced by short-duration and high-intensity rainfall developed from historical small-scale landslides beside the sinuous or meandering reaches or in the source area of rivers. However, most of the large-scale landslides induced by long-duration and high-intensity rainfall were new but were still located beside sinuous or meandering reaches or near the source. The frequency density of landslides under long-duration and high-intensity rainfall was larger by one order than those under short-duration rainfall, and the β values in the landslide frequency density-area analysis ranged from 1.22 to 1.348. The number of downslope landslides was three times larger than those of midslope and upslope landslides. The extreme rainfall-induced landslides occurred in the erosion gullies upstream of the watersheds, whereas those beside rivers were downstream. Analysis of the long-term evolution of landslides in the LRW showed that the geological setting, sinuousness of reaches, and sediment yield volume determined their location and evolution. Small-scale landslides constituted 71.9–96.2% of the total cases from 2003 to 2014, and were more easily induced after Typhoon Morakot (2009). The frequency density of landslides after Morakot was greater by one order than before, with 61% to 68% of total landslides located in the downslope. Small-scale landslides not beside the rivers disappeared within four years, whereas those beside rivers or located in the source areas either developed into large-scale landslides or slowly disappeared. Large-scale landslides caused by Morakot were either combined from several historical small-scale landslides in the river source areas or located beside the sinuous or meandering reaches. The probabilities of landslide recurrence in the LRW during the next 5, 10, and 20 years were determined to be 7.26%, 9.16%, and 10.48%, respectively, and those beside the rivers were 10.47%, 13.33%, and 15.41%, respectively.

Keywords: extreme rainfall; landslide characteristic; landslide frequency density; landslide recurrence probability; sinuous rivers

1. Introduction

Extreme rainfall events occur frequently in Asian countries, including Japan [1,2], Korea [3], India [4], Taiwan [5], and Thailand [6]. Rainfall and earthquakes have been identified as the main triggers of landslides in Taiwan, especially of the extreme rainfall-induced landslide disasters in recent decades. Extreme rainfall-induced disaster events in Taiwan have been catastrophic and powerful, such as the disasters caused by Typhoon Morakot in 2009 [7,8].

Extreme rainfall events in Taiwan are characterized by their increasing intensity [9]; this is one of key factors behind the country's frequent landslide disasters. Extreme rainfall events in Taiwan have still not clearly been defined, but they can be judged as rainfall events with 3-h accumulated rainfall of >130 mm, 6-h accumulated rainfall of >200 mm, or 24-h accumulated rainfall of >350 mm, as based on the analysis of rainfall records from 1992 to 2013 [10]. The number of extreme rainfall events from 2011 to 2015 in the mountainous areas of Nantou County was estimated to be 10 (i.e., twice a year). At the Jiaxian rainfall station in the mountainous areas of Southern Taiwan, the number of monthly rainfall events >1000 mm from 2001 to 2010 was 13, whereas that from 1961 to 1970 was only two. Extreme rainfall events have become a predominant portion of the annual rainfall in Taiwan.

Rainfall-induced landslides can be classified into infiltration-induced slope instability [11–13] and bank-erosion landslides caused by a huge discharge during flooding events [14]. The reasons behind infiltration-induced slope instability include a rising groundwater table or perched water zones near the surface of the slope, reducing the stability of the slope [11]. The groundwater table usually demonstrates an apparent rise during long-duration rainfall events, whereas perched water zones near the slope surface can form during short-duration rainfall events. Bank-erosion landslides represent a considerable portion of extreme rainfall-induced landslide disasters in Taiwan, particularly in the upstream sinuous reaches with extremely large sediment deposition [15].

Most extreme rainfall-induced landslides occurred on hillslopes with angles from 35° to 45°, and were concentrated in valleys or hollow or concave slopes, as revealed by a field investigation of 116 landslides caused by Typhoon Tokage (2004) in Japan [1]. Wu et al. [7] stated that the landslide density induced by extreme rainfall events in the mountainous areas of Taiwan was over 1%, and downslope landslides represented 20.5–39.1% of the total landslide cases in the Kaoping River watershed after Typhoon Morakot.

Rainfall-induced landslide types are related to the rainfall duration. Kung et al. [10] classified short-duration rainfall events as those ≤6 and long-duration rainfall events as those >6 h, based on 22 years of rainfall records in Taiwan. Most landslides caused by short-duration rainfall events in mountainous areas were bank-erosion shallow landslides occurring beside sinuous or meandering reaches with a considerable amount of sediment deposition [15] or occurring in erosion gullies [14]; by contrast, large-scale landslides occurred during long-duration rainfall events, such as the Xiaolin deep-seated landslide that was caused by Typhoon Morakot [8].

Predicting landslide occurrence is critical for the prevention and reduction of landslide disasters. The prediction methods can be classified into two categories according to the landslide types: deep-seated landslide prediction and shallow landslide prediction. Predicting deep-seated landslides usually entails using a hillslope scale and involves locating slopes with landslide potential, setting up instruments to monitor the long-term creeping behavior of the hillslope, and predicting the possible occurrence time of a deep-seated landslide based on the data [16,17]. Most researchers have used light detection and ranging (LIDAR) technology to locate the cliffs of a deep-seated landslide, especially in forested areas [18], to determine the potential hillslope. Predicting shallow landslides usually entails using a watershed scale, and involves determining the landslide characteristics, building shallow landslide susceptibility models based on the landslide characteristics, training and verifying the landslide susceptibility models, and predicting the potential landslide locations [19–21]. The accuracy of landslide susceptibility models is related to the correctness of landslide characteristics.

Considerable efforts have been made to analyze extreme rainfall-induced landslide disasters; however, less attention has been focused on the characteristics of such landslides and the comparison of individual cases. Analyses of rainfall type, landslide distribution, river sinuousness, landslide length-to-width ratio, and landslide recurrence intervals have yet to be discussed in detail. The aims of the current study were to describe and explain the spatial and temporal characteristics of extreme rainfall-induced landslides based on cases from three watersheds in Taiwan. The maximum 24-h accumulated rainfall amounts during Typhoon Morakot (2009) in the Laonong River watershed in Southwest Taiwan, during Typhoon Megi (2010) in the Nanou River watershed in Northeast

Taiwan, and during Typhoon Soudelor (2015) in the Nanshih River watershed in Northern Taiwan exceeded those for a 100-year return period [5]. In this study, we applied landslide inventories that were made in the three aforementioned river watersheds after the mentioned typhoon events to explain the temporal distributions of and differences between the extreme rainfall-induced landslides. Furthermore, we applied landslide inventories that were made in the Laonong River watershed from 2003 to 2014 to explain the spatial distribution and the evolution of rainfall-induced landslides in a landslide-prone watershed.

2. Study Area

2.1. Laonong River Watershed

The Laonong River watershed (hereafter abbreviated as LRW, Figure 1a) has an area of approximately 1380 km^2 with a mean elevation of 1501 m and a mean slope of 33.3°. The river's length is 740.6 km, whereas the river density in the LRW is 0.537 km/km^2. The average annual rainfall varies from 3100.3 mm (Meishan rainfall station, Figure 1a) to 4432.4 mm (Xinan rainfall station, Figure 1a), based on 20 years of records from four rainfall stations (Figure 1a); the rainy season (from May to October) accounts for over 85.0% of the annual rainfall. The constituents of the main strata in the LRW include the Pilushan formation (34.2%), Chaochou formation (29.8%), and Changchihkeng formation (10.4%). The Pilushan formation is of Eocene age, and it consists of slate with metasandstone and igneous rock. The Chaochou formation is of Middle Miocene age, and it consists of argillite and slate intercalated with sandstone lentils. The Changchihkeng formation is of Miocene age, and it consists of alternations of sandstone and shale. Forestry is the main land-use activity, accounting for 83.6% of the watershed area; developed and agricultural areas account for 5.1% and 5.0% of the watershed, respectively.

2.2. Nanou River Watershed

The Nanou River watershed (hereafter abbreviated as NoRW, Figure 1b) has an area of approximately 311.6 km^2, with a mean elevation of 874.9 m and mean slope of 33.3°. The river's length is 167.8 km, whereas the river density in the NoRW is 0.538 km/km^2. The average annual rainfall is 5197 mm, which is based on 20 years of records from the Gulu rainfall station (Figure 1b); the rainy season accounts for between 51.0% and 69.0% of the annual rainfall. The constituents of the main strata in the NoRW include the Kuyuan schist (28.7%), Tungao schist (19.5%), Lushan formation (12.1%), and Nanaoling schist (10.2%). The four main strata are of late Paleozoic to Mesozoic age. The Kuyuan schist consists of phyllite, micaceous schist, and quartz–mica schist, whereas the Tungao schist consists of marble and quartz-mica schist. The Lushan formation consists of slate or phyllite with thin beds of metasandstone, whereas the Nanaoling schist consists of quartz schist and paragneiss. Forestry is the main land-use activity, accounting for 92.8% of the watershed area.

2.3. Nanshih River Watershed

The Nanshih River watershed (hereafter abbreviated as NsRW, Figure 1c) has an area of approximately 255.8 km^2, with a mean elevation of 964.8 m and mean slope of 33.3°. The river's length is 116.0 km, whereas the river density in the NsRW is 0.513 km/km^2. The annual rainfall is 3777 mm, which is based on 20 years of records from the Fushan rainfall station (Figure 1c); the rainy season accounts for between 57.4% and 81.1% of the annual rainfall. The constituents of the main strata in the NsRW include the Tatungshan formation (27.3%), Shuichangliu formation (24.5%), and Kankou formation (21.1%). All three of the main strata are of Oligocene age. The Tatungshan formation consists of argillite intercalated with thin- to thick-bedded siltstone and fine-grained sandstone, whereas the Shuichangliu formation consists of argillite and slate. The Kankou formation consists of argillite or slate intercalated with thin- to thick-bedded siltstone. The NsRW is a low-development watershed area because it is 98.0% occupied by forest.
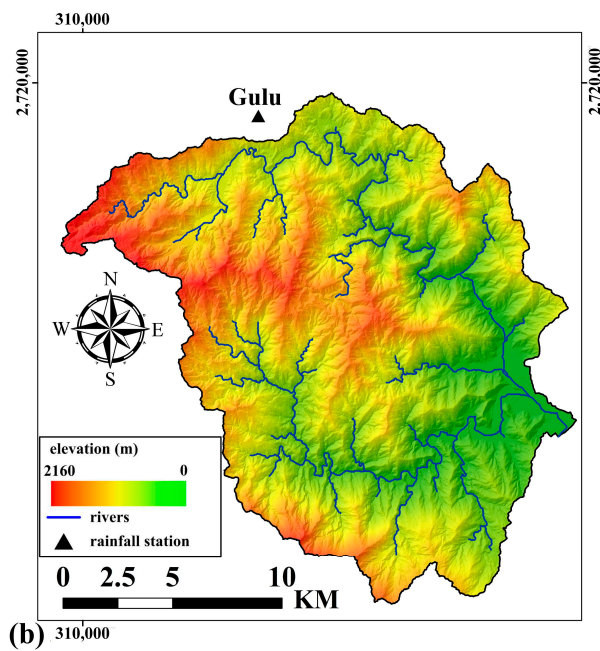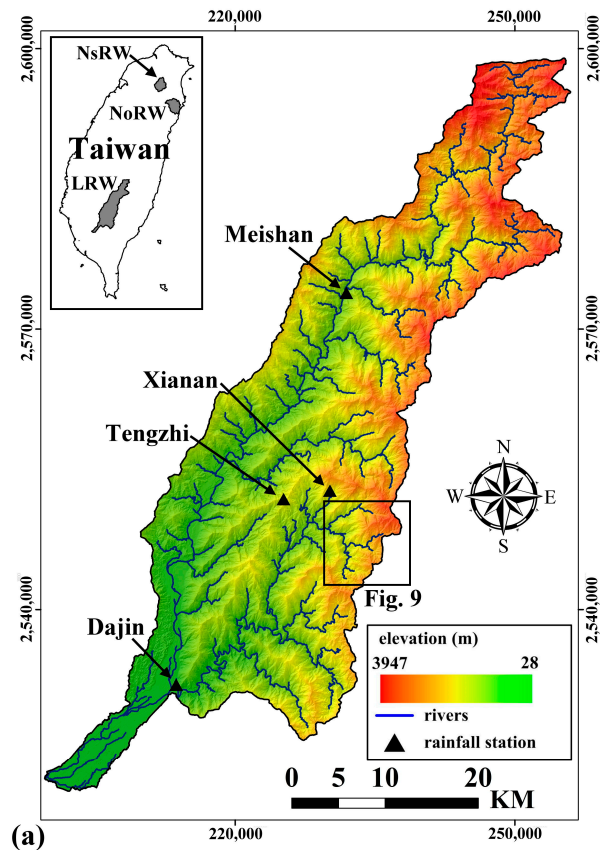
Figure 1. *Cont.*
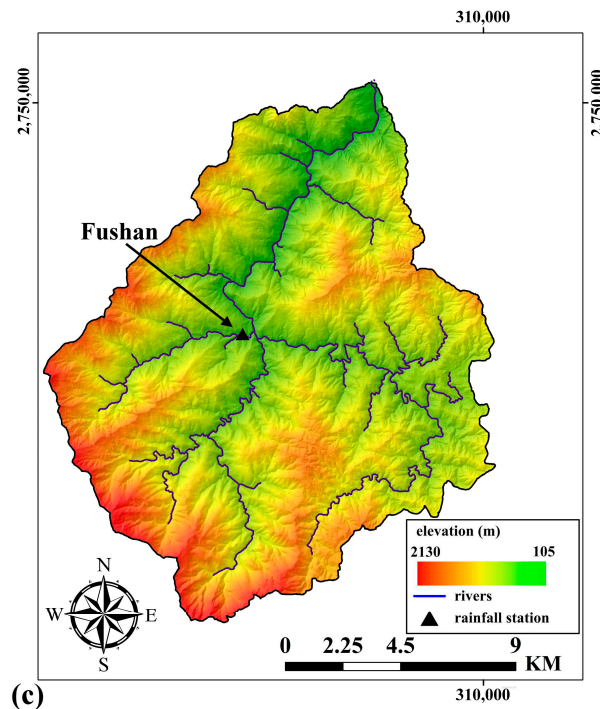
Figure 1. The distribution of elevation, river, and rainfall stations in the Laonong river water (LRW, (**a**)), Nanou river watershed (NoRW, (**b**)), and Nanshih river watershed (NsRW, (**c**)).

3. Materials and Methods

3.1. Materials

Landslides have complex triggers; however, we limited the number of causes to five based on the field survey experience of landslides in Taiwan. The five causes were slope, geological setting, land-use type, river distribution, and accumulated rainfall during typhoon events. A slope mesh was derived from a 5-m digital elevation model (DEM), and the geological setting was extracted from a 1/5000 basin geological map in Taiwan. Land-use investigation maps that were produced in 2008 by the National Land Surveying and Mapping Center were used to analyze the land-use types and distribution. The river distributions were extracted from the 5-m DEM using the Hydrology module in the Spatial Analyst tools of ArcGIS software.

The rainfall records that were used in this study were collected from the representative rainfall stations in the three watersheds. The stations are located in the areas with the highest accumulations of rainfall during typhoon events. We selected the following stations as the representative rainfall stations: the Meishan, Tengzhi, Xinan, and Dajin rainfall stations in the LRW (Figure 1a); the Gulu rainfall station (Figure 1b) in the *NoRW*; and, the Fushan rainfall station in the NsRW (Figure 1c). We used the rainfall records from the Tengzhi rainfall station in the LRW, Gulu rainfall station in the NoRW, and Fushan rainfall station in the NsRW during specific typhoon events to compare extreme rainfall characteristics, as described in Section 4, and the rainfall records from the Meishan, Xinan, and Dajin rainfall stations from 2003 to 2014 in the LRW to explain the long-term rainfall distribution and characteristics, as presented in Section 5.

We used the multiannual landslide inventories that were produced by the Taiwan Forestry Bureau. Landslides were autorecognized using FORMOSAT-2 satellite images with a resolution of 2 m. Because the landslide inventory was autodetected, a few misjudged cases existed in each inventory. We deleted landslides with an area of <25 m^2 or a slope of <15° to reduce the number of misjudged cases. The landslide inventories before and after specific typhoon events in the LRW, NoRW, and NsRW were used, as described in Section 4, and those from 2003 to 2014 in the LRW were used, as described

in Section 5. Landslides with areas > 10^{-1} km², 10^{-1} km² ≥ area > 10^{-2} km², and 10^{-2} km² ≥ area are labeled as large, medium, and small-scale landslides in this paper, respectively.

3.2. Methods

We discuss the spatial distribution and characteristics of extreme rainfall-induced landslides that are associated with specific typhoon events in the three watersheds in Section 4, and we explain the temporal distribution and evolution of rainfall-induced landslides in the LRW in Section 5. Rainfall characteristics were analyzed to compare the landslide-induced strengths of extreme rainfall events. The relationships between landslide distribution and five landslide-related factors were used to explain locations that are prone to extreme rainfall-induced landslides by employing a watershed scale, whereas landslide topographic analyses were used to explain landslide-prone locations by employing a hillslope scale. Landslide frequency density-area distribution analyses were used to compare the frequency densities of various landslide areas in the three watersheds and in the LRW from 2003 to 2014. We also examined the proneness to landslides of sinuous or meandering reaches with sediment yield and deposition in the analyses of the spatial distribution and characteristics of landslides in the three watersheds; furthermore, we examined the long-term evolution and recurrence intervals of landslides in the analyses of the temporal distribution and evolution of landslides in the LRW.

3.2.1. Rainfall Characteristics during Typhoon Events

The characteristics of rainfall events that are considered in this study included rainfall event types, intensity, and duration. We adopted the hourly rainfall records of representative rainfall stations during specific typhoon events to estimate the accumulated rainfall. The period of typhoon events was based on announcements from the Taiwan Central Weather Bureau. The rainfall event types were labeled as extreme rainfall events if the maximum 24-h accumulated rainfall was greater than 350 mm, which is the definition of extreme rainfall in Taiwan (Central Weather Bureau 2015). If the maximum hourly rainfall intensity (abbreviated as R_I) during typhoon events was greater than 70 mm/h, the rainfall events were labeled as high intensity. If the duration of rainfall events was shorter than 6 h or longer than or equal to 6 h, then the rainfall events were labeled as short or long duration, respectively [10]. If the maximum 6-h accumulated rainfall was greater than 420 mm (i.e., mean R_I > 70 mm/h), then the rainfall events were labeled as long duration and high intensity. However, if the maximum 3- and 6-h accumulated rainfall were greater than 210 mm and less than 420 mm, then the rainfall events were labeled as short duration and high intensity.

3.2.2. Landslide Frequency Density-Area Relationship

Several studies have demonstrated that landslide frequency density (N_E) and area (A_E) distributions fit the power-law relationship presented in Equation (1) [22], including landslides in Hong Kong [23], Japan [24], Italy [25], and Taiwan [7]:

$$N_E = \alpha A_E^{-\beta} \tag{1}$$

where α and β are fitting constants. The constant α primarily controls the location of maximum frequency density distribution, whereas the constant β primarily controls the power-law decay for medium and large landslide areas [26]. The constant β is related to landslide-induced factors, geological and terrain characteristics, and whether the landslides are old or new, and is also used to compare the proneness to landslides of various areas around the world. The β value is 2.17 for old landslides in New Zealand [27]; 2.0 for landslides in Coastal California, USA [28]; 1.96 for rainfall-induced landslides in Japan [29]; from 1.3 to 1.4 for extreme rainfall-induced landslides in the Kaoping River watershed in Taiwan [7]; from 1.24 to 1.26 for rainfall-induced landslides in the Shenmu watershed in Central Taiwan [30]; 1.16 for landslides in the central and western regions of New Zealand's Southern Alps [27]; and, 1.11 ± 0.07 based on 172 heavy rainfall-induced landslides from 2006 to 2012 in Taiwan [31].

3.2.3. Topographic Position Analysis

The analysis of the relative position of a landslide on a hillslope, termed topographic position analysis, was suggested by [32] for determining the main inducing factor for landslides. Three parameters were used in the analysis, namely the distance (*a*) from the ridge of the hillslope to the highest point of the landslide, the distance (*b*) from the nearest river at the toe of the hillslope to the lowest point of the landslide, and the total length of the hillslope (*d*). The normalized distances to ridge (*a*/*d*) and to stream (*b*/*d*) were used as dimensionless coordinates (*x*, *y*) of the topographic position analysis plot. Each landslide case in the landslide inventory was plotted according to its relative position on a hillslope by using a circle indicating the area of the landslide. The circles located in the upper-left portion (*a*/*d* < 0.5 and *b*/*d* > 0.5) of the plot meant that the landslides were located near the ridge of the hillslope (termed as upslope landslide), whereas those located in the lower-right portion (*a*/*d* > 0.5 and *b*/*d* < 0.5) of the plot meant the landslides were located near the toe of the hillslope or close to the river (termed as downslope landslide). Circles located in the lower-left portion (*a*/*d* < 0.5 and *b*/*d* < 0.5) of the plot meant that the landslides were located in midslope locations (termed as midslope landslide) and usually had large landslide areas. Most upslope landslides are earthquake-induced [32], whereas most downslope landslides are rainfall- or flood scouring-induced [7,8].

3.2.4. Sediment Yield in the Sinuous or Meandering Reaches

Most typhoon-induced landslides in Taiwan are centralized beside rivers [7], particularly in the sinuous or meandering reaches with active sediment yield and deposition [15]. The sinuosity index (*SI*) can be used to estimate the reaches' sinuousness. The *SI* is the ratio of the length of a curve to the length of the straight line between two end points of the curve, and reaches with $SI = 1.0$, $1.0 < SI \leq 1.5$, and $SI > 1.5$ were labeled as straight reaches, sinuous reaches, and meandering reaches, respectively.

We extracted the river distribution from the 5-m DEM by using the Hydrology toolset in ArcGIS software, but we lowered the threshold value of the river to 3000. The river distributions that are plotted in Figure 1 were extracted with a threshold value of 10,000, and they included main rivers and intermittent streams. However, the river distributions extracted with the river threshold value of 3000 included main rivers, intermittent streams, and ephemeral streams, as well as large and small erosion gullies. Reaches with stream order (*SO*) = 1, 2, 3, 4, ≥5 extracted with the river threshold value of 3000 were labeled as small erosion gullies, large erosion gullies, ephemeral streams, intermittent streams, and main rivers, respectively.

Sediment yield from landslide or debris flow can be estimated from DEMs before and after a rainfall event using airborne LIDAR technology [33–35]. Most studies using LIDAR-extracted DEMs to estimate the sediment yield from landslides have applied a hillslope scale, especially for large-scale landslides [36,37]. Using LIDAR technology to obtain a DEM on a watershed scale remains expensive. We used Equations (2) [38] and (3) [25] to estimate the sediment yield volume from landslides after typhoon events in the three watersheds. In Equations (2) and (3), *A* denotes the total landslide area (m^2) and *V* denotes the total landslide volume (m^3).

$$\ln V = 0.687 \ln A + 2.326 \text{ for landslide area} < 10^6 \text{ m}^2 \ (R^2 = 0.79) \tag{2}$$

$$V = 0.0844 \, A^{1.4324} \text{ for landslide area} \geq 10^6 \text{ m}^2 \ (R^2 = 0.966) \tag{3}$$

3.2.5. Landslide Recurrence Probability

The recurrence probability of earthquake- or rainfall-induced landslides is relative to nature and climate uncertainty. Moreover, the temporal probability of landslide recurrence is difficult to predict [39]; nevertheless, it can be determined using two methods. The first is based on exceedance probability, which is determined using multiannual landslide inventory maps [40] or empirical rainfall thresholds [41], and the second is based on physical models [3,42]. Crovelli [41] suggested that

the continuous-time Poisson model and discrete-time Binomial model can be used to estimate the recurrence exceedance probability of landslides; however, using the discrete-time Binomial model for this estimation in an active occurrence of landslide (i.e., when the mean recurrence intervals are short) can lead to significant overestimation. We used the Poisson model to estimate the landslide recurrence probability under the consideration that landslides occurred frequently and widely in the LRW from 2003 to 2014. The Poisson distribution model was used to predict the occurrence of earthquakes [43], execute landslide hazard estimations [44], and assess the rainfall-triggered landslide recurrence intervals [42,45]. The process of estimating the temporal probability of landslide recurrence using the Poisson distribution model should be conducted in combination with multitemporal landslide inventory maps. The recurrence probability (*P*) of landslides occurring within a specific time interval (*t*) can be estimated using Equation (4):

$$P\{N(t) \geq 1\} = 1 - e^{-t/\mu} \tag{4}$$

where $N(t) \geq 1$ is the exceedance probability and μ is the mean landslide recurrence interval, which should be estimated from multiannual landslide inventories. We utilized the Poisson model with the multiannual landslide inventories from 2003 to 2014 to estimate the landslide recurrence probability in the LRW during the next specific time interval.

4. Characteristics Comparison of Extreme Rainfall-Induced Landslide in the Three Watersheds

4.1. Rainfall Characteristics

The accumulated rainfall distributions in the three watersheds under typhoon events are shown in Figure 2. The accumulated rainfall at the Tengzhi rainfall station during Typhoon Morakot in 2009 (2249.0 mm) was considerably greater than that at the Gulu rainfall station during Typhoon Megi in 2010 (814.0 mm) and that at the Fushan rainfall station during Typhoon Soudelor in 2015 (579.0 mm). The landslide densities in the neighborhood areas of the Tengzhi, Gulu, and Fushan rainfall stations were $0.103/km^2$, $0.0044/km^2$, and $0.0032/km^2$, respectively. The R_I distributions during typhoon events in the three watersheds are shown in Figure 3. The rainfall events in the three watersheds were labeled as extreme torrential rainfall events because the maximum 24-h accumulated rainfall amounts at the Tengzhi, Gulu, and Fushan rainfall stations were 1259.0, 691.5, and 706.0 mm, respectively.

In the LRW, the rainfall type was labeled as long duration and high intensity based on Table 1, whereas, in the NoRW and NsRW, the rainfall types were labeled as short duration and high intensity. The maximum 6-h accumulated rainfall amounts at the Gulu rainfall station (from the 5th to 10th h during Typhoon Megi) and the Fushan rainfall station (from the 39th to 44th h during Typhoon Soudelor) were 101.5 and 349.0 mm, respectively, whereas that at the Tegzhi rainfall station (from the 68th to 73rd hours during Typhoon Morakot) was 1004 mm, which is approximately 9.9 and 2.9 times larger than the amounts at the Gulu and Fushan rainfall stations, respectively.
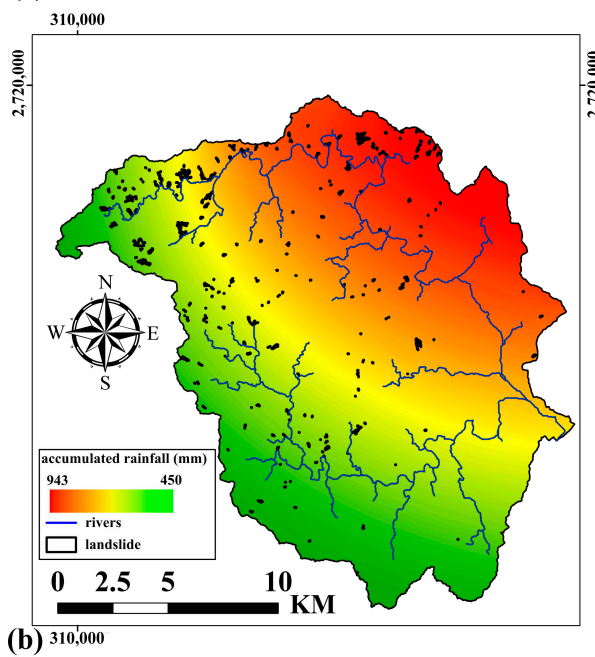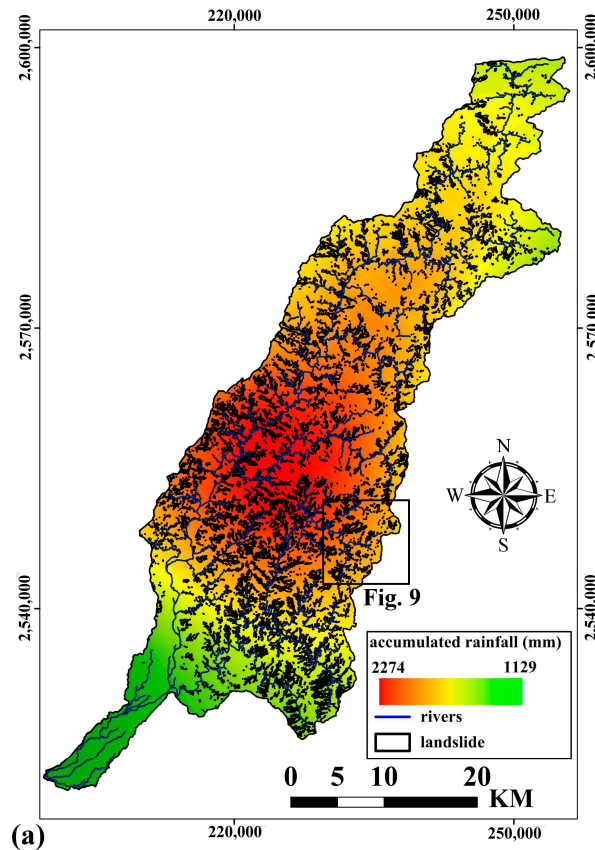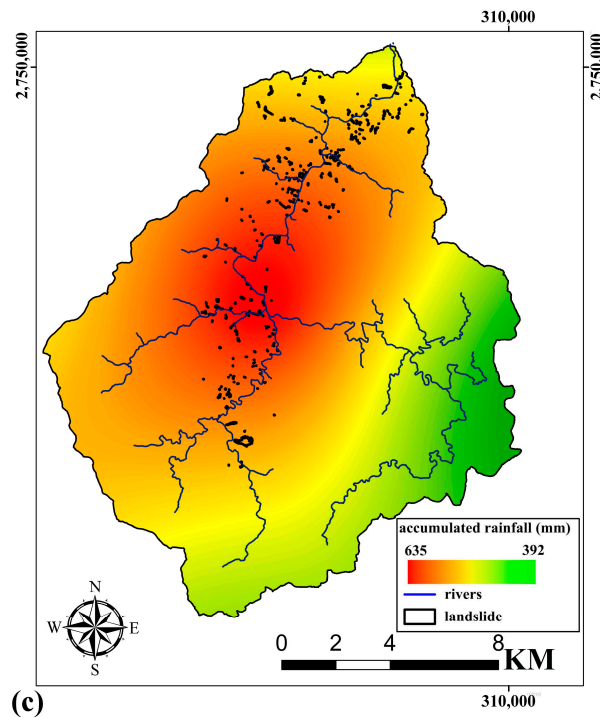
Figure 2. *Cont.*

Figure 2. The distribution of accumulated rainfall during typhoon events and landslide in the LRW (**a**), NoRW (**b**), and NsRW (**c**).
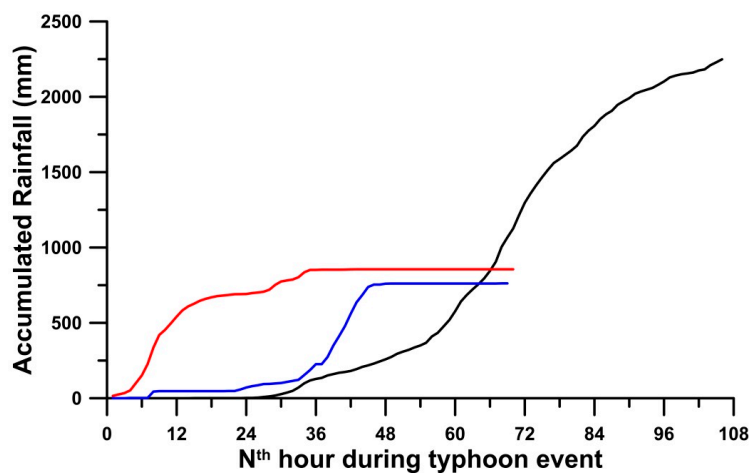

Figure 3. The accumulated rainfall distribution of Tengzhi rainfall station (black line) during 2009 Typhoon Morakot, Gulu rainfall station (red line) during 2010 Typhoon Megi, and Fushan rainfall station (blue line) during 2015 Typhoon Soudelor.

Table 1. The maximum accumulated rainfall at different hours in the three rainfall stations during typhoon events.

Rainfall Station	Typhoon Event	Maximum Accumulated Rainfall (mm) at Different Hour (h)					
		1	3	6	9	12	24
Tengzhi	2009 Typhoon Morakot	99.0	222.0	454.0	622.0	766.0	1259.0
Gulu	2010 Typhoon Megi	109.5	268.5	401.5	531.0	594.5	691.5
Fushan	2015 Typhoon Soudelor	82.0	224.0	412.0	528.0	616.0	706.0

4.2. Relationship between Landslide Distribution and Landslide-Related Factors

Table 2 presents statistical data of the landslide inventories in the three watersheds. The numbers of total landslides and large-scale landslides in the LRW were considerably greater than those in the NoRW and NsRW, as were the landslide densities in the watershed and within 200 m of rivers. The landslide densities within 200 m of rivers in the three watersheds were clearly greater than those in the watersheds, thus implying that landslides caused by extreme rainfall events were strongly centralized beside the rivers.

Table 2. The statistical data of landslide inventories in the three watersheds.

Watersheds	Events	Landslide Numbers		Landslide Density*	
		Total	LSL*	Watershed*	River*
LRW	2009 Typhoon Morakot	7241	215	0.0730	0.241
NoRW	2010 Typhoon Megi	294	1	0.0036	0.223
NsRW	2015 Typhoon Soudelor	342	1	0.0020	0.334

Note: LSL* means large scale landslide. The Landslide Density* (km^2/km^2) is estimated on a watershed scale and within 200 m to rivers.

The distributions of landslide density versus slope in the three watersheds were bell curves, with the highest landslide density being observed in areas with slopes from $30°$ to $40°$ in the LRW ($0.095/km^2$) and from $50°$ to $60°$ in the NoRW ($0.005/km^2$) and NsRW ($0.004/km^2$). This implies that landslides caused by long-duration and high-intensity rainfall events were centralized in the midslope of the hillslopes, whereas those that were caused by short-duration and high-intensity rainfall events were centralized in the upslope of hillslopes.

After Typhoon Morakot, the landslide in the LRW was strongly centralized in the Tangenshan sandstone, Chaochou formation, and Changchihkeng formation. The landslide densities in the three strata were greater than $0.09/km^2$. The similarity between the three strata is that they are of Middle Miocene to Pliocene age and are composed of sandstone. After Typhoon Megi, the landslide in the NoRW was centralized in the Heiyeshan formation, with a landslide density of $0.02/km^2$, and in the Lushan formation, with a landslide density of $0.015/km^2$. The Heiyeshan formation is of Eocene age, whereas the Lushan formation is of Middle Miocene age. The composition in both strata includes metasandstone. After Typhoon Soudelor, the landslide in the NsRW was centralized in the Tsuku formation, with a landslide density of $0.005/km^2$. The Tsuku formation is of Oligocene age and comprises alternations of siltstone and argillite. The extreme rainfall-induced landslide was centralized in the strata composed of sandstone and siltstone.

The landslide density after Typhoon Morakot in the LRW was $0.070/km^2$ in forested areas, $0.033/km^2$ in agricultural areas, and $0.038/km^2$ in developed areas. The landslide density after Typhoon Megi in the NoRW was $0.0018/km^2$ in forested areas, $0.001/km^2$ in agricultural areas, and $0.009/km^2$ in developed areas. The landslide density after Typhoon Soudelor in the NsRW was $0.002/km^2$ in forested areas, $0.010/km^2$ in agricultural areas, and $0.007/km^2$ in developed areas. Therefore, the landslide-prone areas during short-duration and high-intensity rainfall events were the agricultural and developed areas, whereas those during long-duration and high-intensity rainfall events were the forested areas.

4.3. Landslide Frequency Density-Area Distribution

Figure 4 shows the landslide frequency density-area distributions in the three watersheds under typhoon events; the straight lines are the best-fitting lines. The landslide frequency density-area distribution was higher in the LRW than in the NoRW and NsRW on all of the landslide scales; however, the distribution was higher in the NoRW than in the NsRW on medium and large landslide scales. The range of landslide areas for all landslide cases spanned five orders of magnitude from 7×10^{-5} to 3×10^0 km^2 in the LRW, three orders of magnitude from 1×10^{-4} to 9×10^{-2} km^2 in the

NoRW, and four orders of magnitude from 4×10^{-5} to 1×10^{-1} km^2 in the NsRW. Long-duration and high-intensity rainfall events were of higher strength to induce large-scale landslides than short-duration and high-intensity rainfall events.
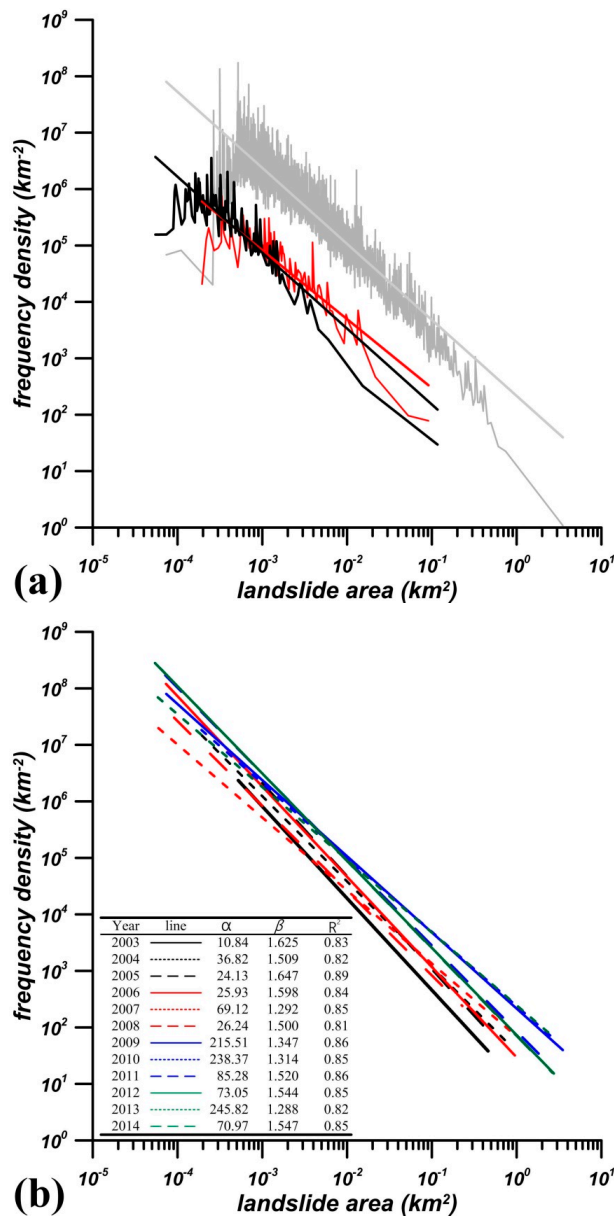

Figure 4. The landslide frequency density-area distribution and fitting lines in the LRW under 2009 Typhoon Morakot (gray line in (**a**)), NoRW under 2010 Typhoon Megi (red line in (**a**)), NsRW under 2015 Typhoon Soudelor (black line in (**a**)), and LRW from 2003 to 2014 (**b**).

The range of landslide areas with the highest frequency density (i.e., the roll-over point) was from 4×10^{-5} to 5×10^{-5} km^2 in the *LRW*, 4×10^{-5} km^2 in the NoRW, and 2×10^{-5} km^2 in the *NsRW*. The frequency densities of small-, medium-, and large-scale landslides were, respectively, from 7×10^4 to 4×10^7 km^{-2}, from 2×10^3 to 6×10^5 km^{-2}, and <7×10^3 km^{-2} in the *LRW*; from 3×10^3 to 5×10^5 km^{-2}, from 1×10^2 to 7×10^3 km^{-2}, and <1×10^3 km^{-2} in the NoRW; and from 9×10^2 to 6×10^6 km^{-2}, from 7×10^1 to 9×10^2 km^{-2}, and <7×10^1 km^{-2} in the NsRW. In the three watersheds, the landslide area with the highest frequency density was from 2×10^{-5} to 5×10^{-5} km^2; however, the frequency density in the LRW was larger than those in the NoRW and NsRW by one to two orders.

The constants α, β, and R^2 of the best-fitting lines in the landslide frequency density-area distribution plot were, respectively, 215.5, 1.348, and 0.86 in the LRW; 17.9, 1.220, and 0.77 in the NoRW; and 6.9, 1.346, and 0.75 in the *NsRW*. The β value in the LRW was higher than those in the NoRW and NsRW. All of the β values in the three watersheds were lower than 1.4, implying that small landslides dominated the landslide inventories in the three watersheds.

4.4. Topographic Position Analysis

Figures 5 and 6 illustrate the topographic position analysis plots in the three watersheds under typhoon events. Table 3 details the statistical data in the three watersheds in the year of typhoon events and in the previous year. The number of downslope landslides in the three watersheds in the year of typhoon events was greater than that in the previous year by 1.03–123.6 times.

Of the total number of landslides in the three watersheds, the percentage of downslope cases ranged from 60% to 77%, whereas that of upslope cases ranged from 18% to 25%. In the three watersheds, the mean areas of downslope landslides after the typhoon events were larger than those of upslope landslides by 1.39–2.01 times, and in the *LRW*, this was larger than those in the NoRW and NsRW by 2.48–5.40 times. The area of downslope landslides that were caused by Typhoon Morakot in the LRW increased by approximately 26.4 km^2, whereas that caused by Typhoon Megi in the NoRW only increased by approximately 0.34 km^2, and that caused by Typhoon Soudelor in the NsRW only increased by approximately 0.02 km^2. The area and number of downslope landslides under long-duration and high-intensity rainfall events were clearly larger than those under short-duration and high-intensity rainfall events.
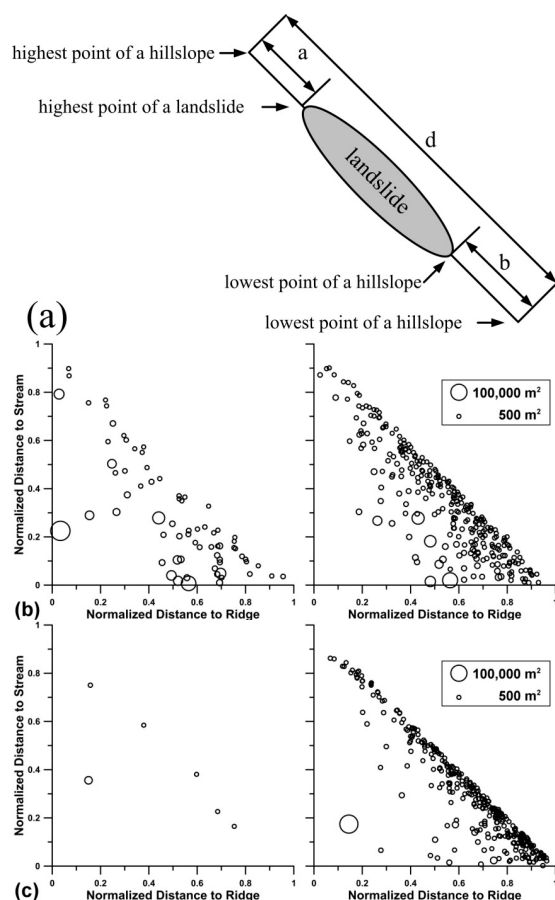

Figure 5. The schematic map of landslide position analysis (**a**); revised from [30] and the landslide position analysis plots in the NoRW in 2009 (left figure in (**b**)) and 2010 (right figure in (**b**)), and in the NsRW in 2014 (left figure in (**c**)) and 2015 (right figure in (**c**)).
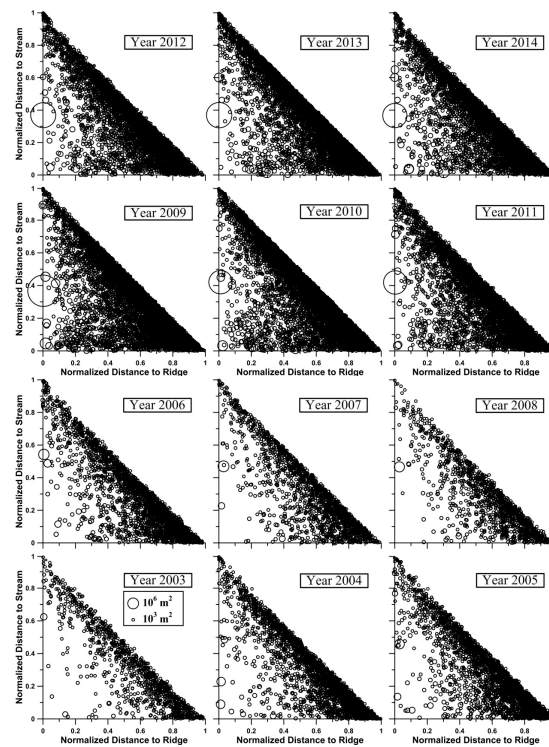
Figure 6. The landslide position analysis plots in the LRW from 2003 to 2014.

Table 3. The statistical data of upslope, downslope, and midslope landslide cases in the three watersheds.

Locations	NoRW in 2009			NoRW in 2010			NsRW in 2014		
	N*	Per*	TA*	N	Per	TA	N	Per	TA
DS*	41	59	481,925	176	60	498,944	2	33	2744
US*	14	20	117,475	72	25	132,040	3	50	1784
MS*	15	21	338,925	46	16	543,287	1	17	29,292
	NsRW in 2015			LRW in 2003			LRW in 2004		
DS*	262	77	339,194	655	61	3,450,660	1710	67	9,436,217
US*	60	18	38,655	243	23	1,976,064	463	18	2,222,163
MS*	20	6	73,557	169	16	2,993,968	383	15	9,848,955
	LRW in 2005			LRW in 2006			LRW in 2007		
DS*	1837	68	11,606,038	1737	67	10,845,901	1044	63	6,794,636
US*	429	16	3,138,360	456	18	3,705,787	334	20	1,310,816
MS*	432	16	11,820,557	411	16	12,163,322	276	17	7,752,975
	LRW in 2008			LRW in 2009			LRW in 2010		
DS*	701	66	5,536,640	2851	63	31,906,507	4786	62	29,548,656
US*	163	15	1,122,250	867	19	6,121,908	1741	23	5,411,773
MS*	196	19	5,996,833	822	18	62,622,404	1143	15	49,371,784
	LRW in 2011			LRW in 2012			LRW in 2013		
DS*	3007	61	24,183,843	2985	62	22,509,769	4338	63	22,058,529.7
US*	981	20	6,037,161	942	20	5,046,249	1640	24	5,653,749.2
MS*	961	19	38,732,913	903	19	32,738,814	941	14	33,581,493.8
	LRW in 2014								
DS*	2893	62	22,278,709						
US*	885	19	6,128,770						
MS*	899	19	34,599,337						

Note: N*, Per*, and TA* mean the number of landslide case, the percentage (%) of landslide case number to the total landslide case number, and the total area (m^2) of landslide cases. DS*, US*, and MS* mean the downslope, upslope, and midslope landslide.

4.5. Locations of Extreme Rainfall-Induced Landslides

Sediment yield from landslides or debris flow is highly active in the mountainous areas of Taiwan, and extremely large sediment deposition in the upstream reaches results in severe bank-erosion landslides in sinuous or meandering reaches. Table 4 shows the statistical data of landslide distribution in reaches with different *SO* values in the three watersheds after typhoon events. If the lowest points of landslides were within 200 m of rivers, the cases were recognized as being located beside rivers. Of the total watershed area, the percentage of areas within 200 m to rivers was only 41.0–42.6% in the three watersheds; however, of the total number of landslides after typhoon events, the percentage of landslides beside rivers was 90.9–95.0%. Of the total number of landslides, the percentage of landslides beside small and large erosion gullies and ephemeral streams was 75.8–82.8% in the three watersheds, whereas, the percentage of those beside main rivers and intermittent streams was 10.8–19.3%. Most extreme rainfall-induced landslides were centralized beside erosion gullies and ephemeral streams. The mean landslide densities in the areas within 200 m of reaches with *SO* values of 1, 2, 3, 4, 5, and 6 were, respectively, $0.187/km^2$, $0.142/km^2$, $0.135/km^2$, $0.121/km^2$, $0.112/km^2$, and $0.079/km^2$ in the LRW; $0.012/km^2$, $0.008/km^2$, $0.007/km^2$, $0.007/km^2$, $0.005/km^2$, and $0.003/km^2$ in the NoRW; and $0.007/km^2$, $0.006/km^2$, $0.005/km^2$, $0.005/km^2$, $0.003/km^2$, and $0.002/km^2$ in the NsRW. The landslide density in the upstream reaches was larger than that in the downstream reaches; moreover, in the watersheds, the landslide density after long-duration and high-intensity rainfall events was larger than that after short-duration and high-intensity events.

Table 4. The ratio of the number of landslide beside the reaches with different stream order (*SO*) to the total number of landslide induced by typhoon events in the three watersheds.

Watersheds	*SO* Value of the Reache							Total Percentage
	1	2	3	4	5	6	7	
LRW	34.7	31.7	13.4	6.4	3.2	1.5	0.0	90.9
NoRW	51.7	22.0	9.1	5.1	5.7	0.0	-	93.6
NsRW	40.4	19.0	16.4	9.4	7.3	2.6	-	95.0

Figure 7 shows the mean *SI* value in reaches with various *SO* values in the three watersheds. The mean *SI* value in reaches with *SO* values of ≤3 ranged from 1.08 to 1.13 in the LRW, 1.10 to 1.16 in the NoRW, and 1.08 to 1.15 in the NsRW. The mean *SI* value in reaches with *SO* values of ≥4 was greater than 1.50 and peaked in reaches with *SO* = 6 in the LRW; moreover, the mean *SI* value ranged from 1.37 (reaches with *SO* = 6) to 3.11 (reaches with *SO* = 5) in the NoRW and from 1.51 (reaches with *SO* = 6) to 1.95 (reaches with *SO* = 4) in the NsRW. The reaches with *SO* values of ≤3 in the three watersheds are sinuous reaches, whereas those with *SO* values of >4 are meandering reaches.
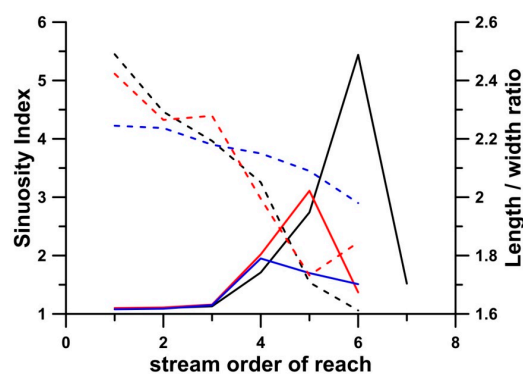

Figure 7. The mean sinuosity index (black line for LRW, red line for NoRW, and blue line for NsRW) of and length/width ratio (black dash line for LRW, red dash line for NoRW, and blue dash line for NsRW) of landslide cases in the three watersheds.

Sediment yield from the landslides and deposition in the upstream reaches was a key difference in the three watersheds. The total landslide volume was estimated as 650.33×10^6 m^2 after Typhoon Morakot in the LRW, 0.134×10^6 m^2 after Typhoon Megi in the NoRW, and 0.078×10^6 m^2 after Typhoon Soudelor in the NsRW, based on Equations (3) and (4). The total landslide volume after Typhoon Morakot in the *LRW* was over 4000 times larger than those in the NoRW and NsRW. Most of the sediment from the rainfall-induced landslides was deposited in the upstream reaches, especially in the sinuous or meandering reaches. The mean sediment deposition depth after Typhoon Morakot in the Laonong River was recorded as >10 m [46], whereas those after Typhoon Megi in the Nanou River and Typhoon Soudelor in the Nanshih River were recorded as only <1.5 m. Abundant sediment deposition in the sinuous or meandering reaches resulted in severe bank-erosion landslides during heavy rainfall events. Extremely large amounts of sediment were yielded from abundant infiltration-induced landslides in the upstream regions and deposited or transported to the sinuous or meandering reaches. The peak discharge under long-duration and high-intensity rainfall events in the LRW was larger than those under short-duration and high-intensity events in the NoRW and NsRW. The larger peak discharge resulted in more landslides beside the sinuous and meandering reaches in the LRW than in the NoRW and NsRW.

The length-to-width ratio (*L/W* ratio) of landslides can facilitate explaining their inducing mechanisms [47] and their shape characteristics [48]. Landslides induced by river scouring usually exhibit low *L/W* ratios, whereas those induced by infiltration exhibit high *L/W* ratios. Figure 7 shows the mean *L/W* ratios of landslides beside the reaches with various *SO* values. The mean *L/W* ratios of landslides in all reaches ranged from 1.612 to 2.490 in the LRW, 1.845 to 2.423 in the NoRW, and 1.98 to 2.245 in the NsRW. The ranking of the mean *L/W* ratio difference of landslides beside the reaches with *SO* values of 1 and 6 in the three watersheds (i.e., 0.878 in the LRW, 0.578 in the NoRW, and 0.265 in the NsRW) was the same as the ranking of sediment yield that was caused by typhoon events in the three watersheds. The mean *L/W* ratio of landslides beside the reaches with *SO* = 1 in the LRW was the highest among the three watersheds, whereas that of landslides beside the reaches with *SO* = 6 in the LRW was the lowest. Therefore, sediment yield in the LRW was a key influencing factor for landslides. Landslides with low *L/W* ratios that were occurring beside the reaches with *SO* values of >3 were induced by the river scouring the hillslopes beside the sinuous or meandering reaches, whereas those with high *L/W* ratios that were occurring beside the reaches with *SO* values of ≤3 were induced by infiltration, which developed in the erosion gullies.

5. Long-Term Evolution of Landslides from 2003 to 2014 in the LRW

5.1. NUMBER of Landslides and Characteristics of Rainfall Type

Figure 8 shows the statistical data of rainfall records from 2003 to 2014 in the LRW. The mean annual rainfall from 2003 to 2014 ranged from 3100 to 4432 mm at the Meishan, Xinan, and Dajin rainfall stations (Figure 1), whereas that for the whole of Taiwan was reported to be approximately 2500 mm. The mean times per year of daily rainfall (R_D) > 350 mm from 2003 to 2014 at the three rainfall stations was 0.83–2.25, whereas that of R_I > 70 mm/h was 0.33–1.53. The number of small-, medium-, and large-scale landslides constituted 71.9–96.2%, 2.0–24.0%, and <5.0% of the total number of landslides from 2003 to 2014, respectively. From 2003 to 2014, the total numbers of landslides and small-scale landslides were the highest in 2010 and the lowest in 2008, whereas those of medium- and large-scale landslides were the highest in 2009 and the lowest in 2008.

Two ascending sections in the numbers of landslide from 2003 to 2014, which are from 2008 to 2010 and 2012 to 2013, are shown in Figure 8. In the LRW, the total numbers of landslides, small-scale landslides, medium-scale landslides, and large-scale landslides were, respectively, 3480, 2243, 1068, and 170 from 2008 to 2009, and were 3131, 3200, −52, and −20 from 2009 to 2010. Therefore, the total number landslides increased in the year of Typhoon Morakot; however, only small-scale landslides increased in the year after Morakot. The mean annual rainfall, total times of R_D > 350 mm,

and total times of $R_I > 70$ mm/h at the three rainfall stations in 2009 (3629.0 mm) were 3629.0 mm, 7, and 8, respectively, whereas those in 2010 were 3070.0 mm, 2, and 1, respectively. The increases in small-, medium-, and large-scale landslides from 2012 to 2013 were 2121, −25, and −7, respectively. The mean annual rainfall, total times of $R_D > 350$ mm, and total times of $R_I > 70$ mm/h in 2012 were 4319.0 mm, 4, and 3, respectively, whereas those in 2013 were 3238.0 mm, 1, and 1, respectively. In the LRW, small-scale landslides were more easily induced after Typhoon Morakot than before Morakot. Moreover, the occurrences of medium- and large-scale landslides were more relative to the total times per year of $R_D > 350$ mm and $R_I > 70$ mm/h than to annual rainfall, particularly in the years with total times per year of >9.
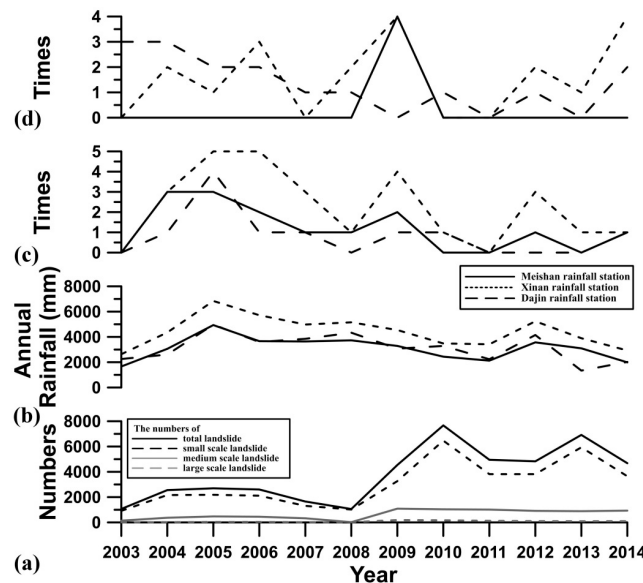

Figure 8. The numbers of landslide (**a**), including total landslide (black line), small scale landslide (black dash line), medium scale landslide (grey line), and large scale landslide (grey dash line) and annual rainfall (**b**), the times of $R_D > 350$ mm (the standard of heavy rainfall, (**c**), and the times of $R_I > 70$ mm/h (**d**) according to the records of Meishan (black line), Xinan (black point line), and Dajin (black dash line) from 2003 to 2014 in the LRW.

5.2. The Landslide Frequency Density-Area Distribution

Figure 5b shows the landslide frequency density-area distribution from 2003 to 2014. The range of landslide areas for total landslides spanned less than six orders of magnitude from 5×10^{-5} to 2×10^1 km^2 from 2003 to 2008, which enlarged to seven orders of magnitude from 5×10^{-5} to 3×10^2 km^2 in 2009 (the maximum span from 2003 to 2014), and narrowed to seven orders of magnitude from 4×10^{-5} to 2×10^2 km^2 in 2013.

The β value of the best-fitting line in the landslide frequency density-area distribution plot from 2003 to 2014 ranged from 1.288 (in 2013) to 1.647 (in 2005). The difference in the β value was −0.153 from 2008 to 2009 and −0.256 from 2012 to 2013. The frequency densities in landslide areas of 10^{-2} and 10^{-1} km^2 in 2008 were 2×10^5/km^2 and 9×10^2/km^2, increasing to 1×10^6/km^2 and 8×10^3/km^2 in 2009. The frequency densities in landslide areas of 10^{-2} and 10^{-1} km^2 from 2009 to 2014 were never smaller than 8×10^5/km^2 and 4×10^3/km^2. This result indicates that a rainfall event with the return period of >200 years (i.e., Typhoon Morakot in 2009) could raise the frequency density of landslides by one order in the LRW, and that the frequency density of landslides was never smaller than the original frequency density in 2008 from 2010 to 2014.

In the LRW, the decline in the β value from 2012 to 2013 was greater than that from 2008 to 2009, and the β value in 2013 was the lowest from 2003 to 2014. This is because the increase in the number

of small-scale landslides from 2012 to 2013 was a dominant portion of the increase in the number of total landslides.

5.3. Topographic Position Analysis

Figure 6 and Table 3 show the topographic position analysis plot and the statistical data from 2003 to 2014 in the LRW, respectively. Downslope landslides constituted 61–68% of the total landslides from 2003 to 2014, whereas upslope and midslope landslides constituted 15–24% and 14–19%, respectively. The total area of downslope landslides ranged from 3.45×10^6 to 5.53×10^6 m^2 from 2003 to 2008, increasing to 31.9×10^6 m^2 in 2009, and was never smaller than 22.0×10^6 m^2 from 2010 to 2014. The total area of midslope and upslope landslides had similar trends with that of small-scale landslides.

The area and number of downslope landslides in the LRW were relative to the total times per year of $R_D > 350$ mm and $R_I > 70$ mm/h at the three rainfall stations. In the LRW, the area and number of downslope landslides from 2003 to 2014 reached a peak in 2009; moreover, the total times per year of $R_D > 350$ mm and $R_I > 70$ mm/h at the three rainfall stations from 2003 to 2014 also reached a peak in 2009. The area and number of downslope, upslope, and midslope landslides had a rising trend as the total times per year of $R_D > 350$ mm and $R_I > 70$ mm/h at the three rainfall stations were over nine.

5.4. Long-Term Evolution of Landslides

We applied the multiyear landslide distribution derived in a subwatershed (Figures 1 and 9) to explain the long-term evolution of landslides in the *LRW*. No large-scale landslide case occurred in the subwatershed of the LRW from 2003 to 2007. The location of landslides caused by Typhoon Morakot can be classified into three types: not beside rivers, beside rivers, and in the source area of rivers. The small landslides not located beside rivers gradually disappeared (i.e., through vegetation recovery) within four years. The landslides located beside rivers, especially the sinuous or meandering reaches (red rectangle in Figure 9), either developed gradually into large-scale landslides or disappeared slowly. The landslides located in the source area of rivers (red circle in Figure 9) gradually developed into large-scale landslides. The locations of the large-scale landslides caused by Typhoon Morakot could be verified in the aforementioned analyses. The large-scale landslides that were caused by Typhoon Morakot occurred only in two locations. The first was in a source area of a river and was a combination of several historical small-scale landslides (red circle in Figure 9). The second was beside a sinuous or meandering reach (red circle in Figure 9).
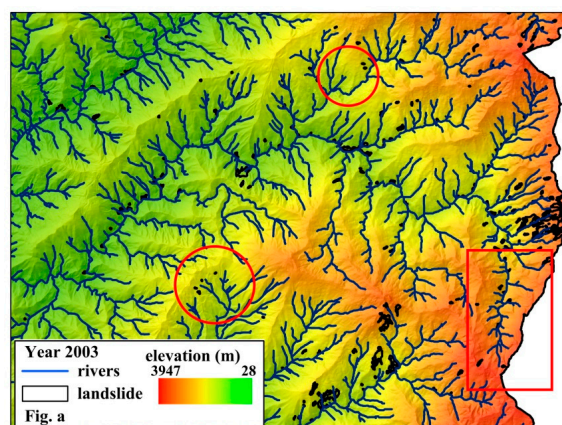

Figure 9. *Cont.*
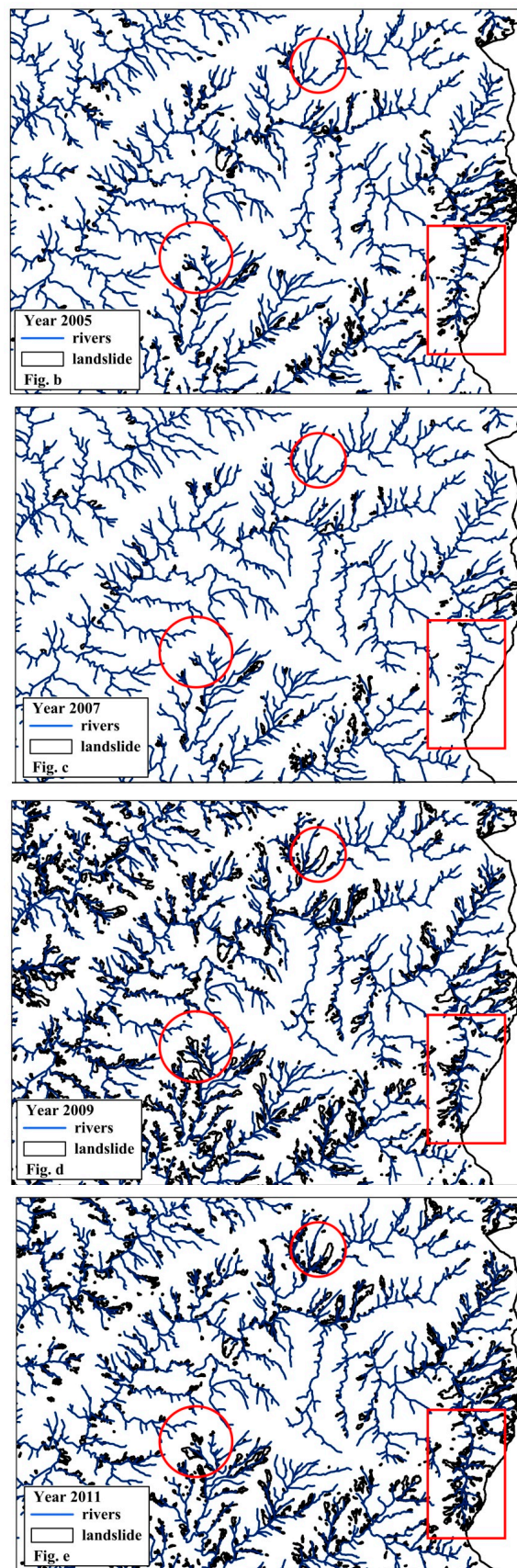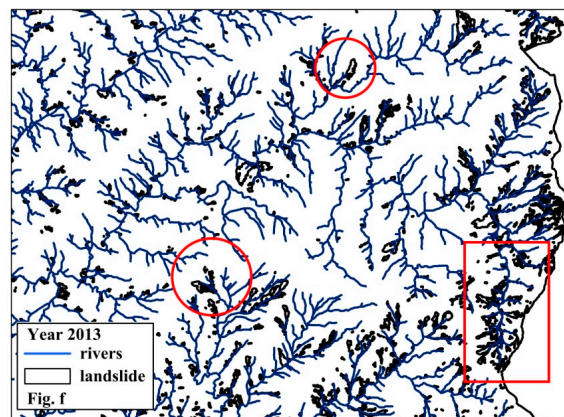
Figure 9. *Cont.*

Figure 9. The long-term evolution of landslide in a sub-watershed of LRW (Figures 1 and 2) from 2003 to 2013.

5.5. Mean Recurrence Interval of Landslides

We used the Poisson model to estimate the probability of landslide recurrence based on the multiannual landslide inventories from 2003 to 2014 in the LRW. The total times that a 5-m grid was recognized as a landslide in 12 years were used to estimate the mean recurrence interval in a specific time interval. The areas of grids recognized as landslide grids for ≥ 1 time, ≤ 5 times, and >5 times from 2003 to 2014 in the LRW were 153.4 km^2 (11.1% of the watershed area), 113.9 km^2 (8.3% of the watershed area), and 39.5 km^2 (2.9% of the watershed area), respectively. Approximately 88.9% of the watershed area had never been recognized as landslide grids in 12 years in the LRW. The mean number of times that grids had been recognized as landslides in 12 years in the LRW was 0.39.

If the grids had never been recognized as landslides from 2003 to 2014, the total time of landslide occurrence was 0; however, we used 0.001 instead of 0 to avoid a calculation with no meaning. Figure 9 shows the probability distribution of landslide recurrence during the next 5, 10, and 20 years in the *LRW*. The mean probabilities of landslide recurrence during the next 5, 10, and 20 years in the *LRW* (Figure 10) were determined to be 7.26%, 9.16%, and 10.48%, respectively, whereas those in the area within 200 m of rivers were 10.47%, 13.33%, and 15.41%, respectively.

Figure 10d shows the probability distribution of landslide recurrence during the next specific time interval in the LRW. The landslide recurrence probability of grids that were never recognized as landslides in 12 years was calculated to range from 0.0% to 1.65% during the subsequent 1 to 200 years. The recurrence probability of grids that were recognized as landslides for ≥ 1 time ranged from 8.0% to 63.2% during the subsequent year, but it ranged from 56.5% to 100.0% during the subsequent 10 years and was close to 100.0% during the subsequent 100 years.
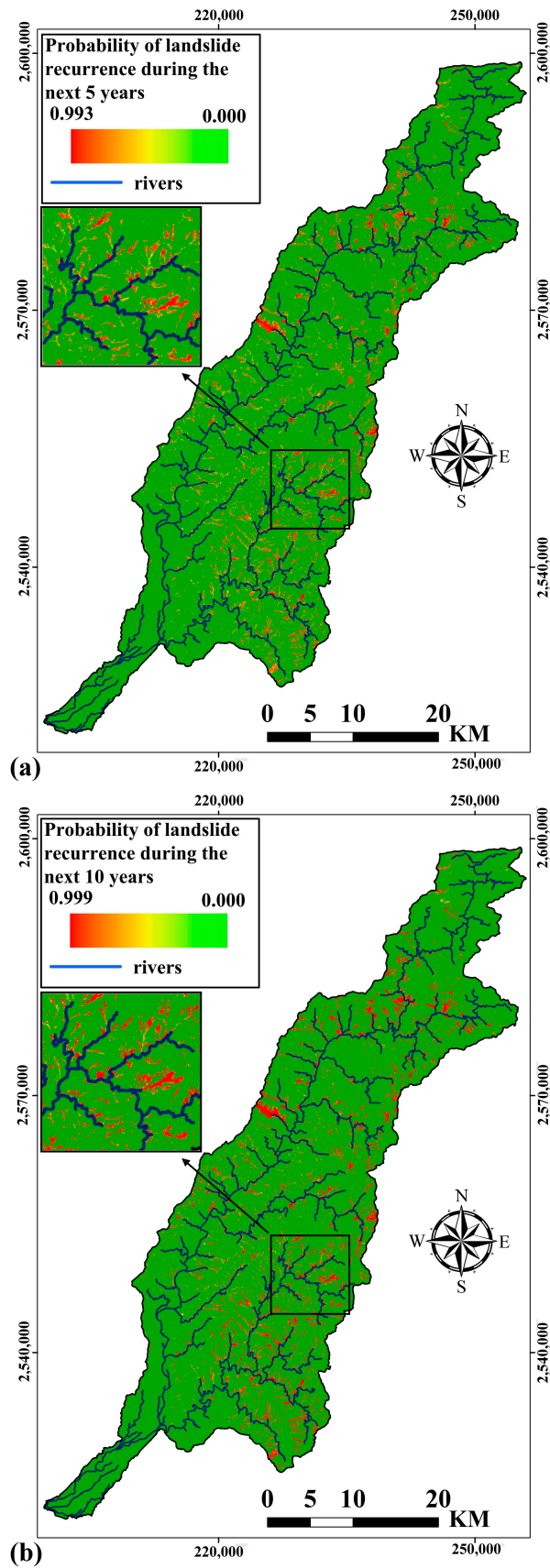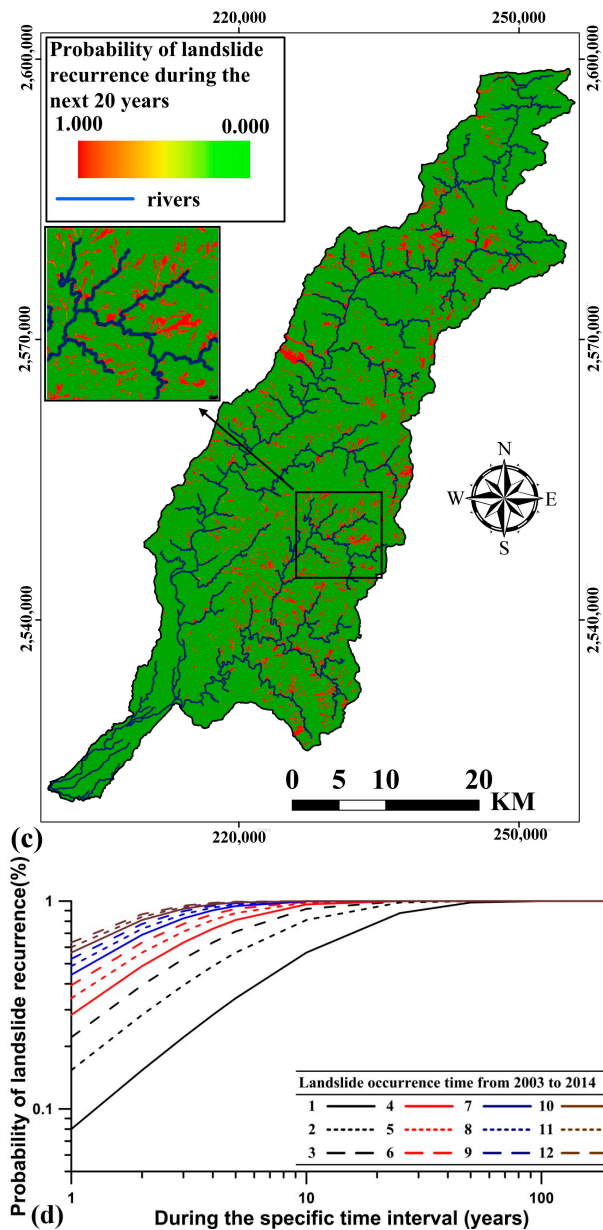
Figure 10. *Cont.*

Figure 10. The probability distribution of landslide recurrence during the next 5 (**a**), 10 (**b**), and 20 (**c**) years in the LRW. (**d**) Explains the landslide recurrence probability during the next specific time interval based on the landslide occurrence time from 2003 to 2014 in the LRW.

6. Conclusions

We demonstrated the characteristics of extreme rainfall-induced landslides based on three landslide inventories after typhoon events in three watersheds. Some conclusions can be made based on the analysis results. Most extreme rainfall-induced landslides were centralized in areas with strata consisting of sandstone and siltstone. The landslide-prone areas under short-duration and high-intensity rainfall events were agricultural and developed areas, whereas those under long-duration and high-intensity events were forested areas. Large-scale landslides were most likely induced by rainfall events with maximum 6-h accumulated rainfall amounts of over 420 mm. The highest landslide frequency density in the LRW was 5×10^6/km^2 in landslide areas of 2×10^{-5} to 5×10^{-5} km^2, whereas those in the NoRW and NsRW were only 1×10^5/km^2 and 6×10^5/km^2 in the same landslide areas. The β values of the landslide frequency density-area analysis that were associated

with extreme rainfall events in the three watersheds were lower than 1.348; therefore, small-scale landslides were a dominant portion of the total landslides. The number of downslope landslide cases constituted 60–77% of the total landslides in the extreme rainfall-induced landslide inventories. Moreover, 90.9–95.0% of the total landslides centralized beside the sinuous or meandering reaches, and extremely large sediment deposition in these reaches resulted in severe bank-erosion landslides.

We also explained the long-term evolution of landslides in the LRW based on the multiannual landslide inventories. The number of small-scale landslides constituted a dominant portion (71.9–96.2%) of total landslides in 12 years, whereas those of medium- and large-scale landslides constituted only 2.0–24.0% and <5.0%, respectively. Medium- and large-scale landslides occurred only in the years in which the total times per year of R_D > 350 mm and R_I >70 mm/h were over nine. The frequency density of landslides after Typhoon Morakot rose by one order of magnitude when compared with that before Morakot, and never fell to the original frequency density of landslides in 2008 in the five years following Morakot. Of the total landslides in 12 years, downslope, midslope, and upslope landslides constituted 61–68%, 15–24%, and 14–19%, respectively. Furthermore, small-scale landslides in the LRW that were not beside rivers disappeared within four years, whereas those beside rivers or in source areas either developed into large-scale landslides or disappeared slowly. Large-scale landslides in the LRW were only located in the source area of rivers combined with several historical small-scale landslides or beside the sinuous or meandering reaches. We used the Poisson model to estimate landslide recurrence probabilities in the LRW, which, during the next 5, 10, and 20 years, were 7.26%, 9.16%, and 10.48%, respectively, whereas those beside rivers were 10.47%, 13.33%, and 15.41%, respectively.

Conflicts of Interest: The author declares no conflicts of interest.

References

1. Dahal, R.K.; Hasegawa, S.; Nonomura, A.; Yamanaka, M.; Masuda, T.; Nishino, K. Failure characteristics of rainfall-induced shallow landslides in granitic terrains of Shikoku Island of Japan. *Environ. Geol.* **2009**, *56*, 1295–1310. [CrossRef]
2. Tsuchida, T.; Athapaththu, A.M.R.G.; Hanaoka, T.; Kawaguchi, M. Investigation of landslide calamity due to torrential rainfall in Shobara City, Japan. *Soils Found.* **2015**, *55*, 1305–1317. [CrossRef]
3. Vasu, N.N.; Lee, S.R.; Pradhan, A.M.S.; Kim, Y.T.; Kang, S.H.; Lee, D.H. A new approach to temporal modelling for landslide hazard assessment using an extreme rainfall induced-landslide index. *Eng. Geol.* **2016**, *215*, 36–49. [CrossRef]
4. Kumar, A.; Asthana, A.; Priyankab, R.S.; Jayangondaperumal, R.; Gupta, A.K.; Bhakuni, S.S. Assessment of landslide hazards induced by extreme rainfall event in Jammu and Kashmir Himalaya, northwest India. *Gemorphology* **2017**, *284*, 72–87. [CrossRef]
5. Chou, H.T.; Lee, C.F.; Lo, C.M.; Lin, C.P. Landslide and alluvial fan caused by an extreme rainfall event in Suao, Taiwan. In Proceedings of the 11th International and 2nd North American Symposium on Landslides, Banff, AB, Canada, 3–8 June 2011.
6. Ono, K.; Kazama, S. Analyses of extreme daily rainfall in Southeast Asia with a gridded daily rainfall data set. In Proceedings of the Symposium Hydro-Climatology: Variability and Change, Melbourne, Australia, 4–6 July 2011; pp. 169–175.
7. Wu, C.H.; Chen, S.C.; Chou, H.T. Geomorphologic Characteristics of Catastrophic Landslides during Typhoon Morakot in the Kaoping Watershed, Taiwan. *Eng. Geol.* **2011**, *123*, 13–21. [CrossRef]
8. Wu, C.H.; Chen, S.C.; Feng, Z.Y. Formation, failure, and consequences of the Xiaolin landslide dam, triggered by extreme rainfall from Typhoon Morakot, Taiwan. *Landslides* **2014**, *11*, 357–367. [CrossRef]
9. Shiu, C.J.; Liu, S.C.; Chen, J.P. Diurnally asymmetric trends of temperature, humidity, and precipitation in Taiwan. *J. Clim.* **2009**, *22*, 5635–5649. [CrossRef]

10. Kung, C.Y.; Yen, B.L.; Li, C.R.; Wu, Y.Z.; Yu, Y.C. *The Rank of Extreme Rainfall Events over Taiwan*; National Science and Technology Center for Disaster Reduction: New Taipei City, Taiwan, 2015.

11. Collins, B.D.; Znidarcic, D. Stability analyses of rainfall induced landslides. *J. Geotech. Geoenviron. Eng.* **2004**, *130*, 362–372. [CrossRef]

12. Conte, E.; Troncone, A. A method for the analysis of soil slips triggered by rainfall. *Géotechnique* **2012**, *62*, 187–192. [CrossRef]

13. Conte, E.; Donato, A.; Troncone, A. A simplified method for predicting rainfall-induced mobility of active landslides. *Landslides* **2017**, *14*, 35–45. [CrossRef]

14. Lyn, L.; Wang, Z.Y.; Cui, P.; Xu, M.Z. The role of bank erosion on the initiation and motion of gully debris flows. *Geomorphology* **2017**, *285*, 137–151. [CrossRef]

15. Chen, S.C.; Wu, C.H.; Chao, Y.C.; Shih, P.Y. Long-term impact of extra sediment on notches and incised meanders in the Hoshe River, Taiwan. *J. Mt. Sci.* **2013**, *10*, 716–723. [CrossRef]

16. Klimeš, J.; Yepes, J.; Becerril, L.; Kusák, M.; Galindo, I.; Blahut, J. Development and recent activity of the San Andrés landslide on El Hierro, Canary Islands, Spain. *Geomorphology* **2016**, *261*, 119–131. [CrossRef]

17. Stemberk, J.; Hartvich, F.; Blahůt, J.; Rybář, J.; Krejčí, O. Tectonic strain changes affecting the development of deep seated gravitational slope deformations in the Bohemian Massif and Outer Western Carpathians. *Geomorphology* **2017**, *289*, 3–17. [CrossRef]

18. Van Den Eeckhaut, M.; Kerle, N.; Poesen, J.; Hervás, J. Object-oriented identification of forested landslides with derivatives of single pulse LiDAR data. *Geomorphology* **2012**, *173–174*, 30–42. [CrossRef]

19. Crozier, M.J. A proposed cell model for multiple-occurrence regional landslide events: Implications for landslidesusceptibility mapping. *Geomorphology* **2017**, *295*, 480–488. [CrossRef]

20. Jumar, D.; Thakur, M.; Dubey, C.S.; Shukla, D.P. Landslide susceptibility mapping & prediction using Support Vector Machine for Mandakini River Basin, Garhwal Himalaya, India. *Geomorphology* **2017**, *295*, 115–125. [CrossRef]

21. Zêzere, J.L.; Pereira, S.; Melo, R.; Oliveira, S.C.; Garcia, R.A.C. Mapping landslide susceptibility using data-driven methods. *Sci. Total Environ.* **2017**, *589*, 250–267. [CrossRef] [PubMed]

22. Bak, P.; Tang, C.; Wiesenfeld, K. Self-organized criticality. *Phys. Rev. A* **1988**, *38*, 364–374. [CrossRef]

23. Dai, F.C.; Lee, C.F. Frequency-volume relation and prediction of rainfall-induced landslides. *Eng. Geol.* **2001**, *59*, 253–266. [CrossRef]

24. Turcotte, D.L.; Malamud, B.D. Landslides, forest fires, and earthquakes: Examples of self-organized critical behavior. *Phys. A Stat. Mech. Appl.* **2004**, *340*, 580–589. [CrossRef]

25. Guzzetti, F.; Ardizzone, F.; Cardinali, M.; Galli, M.; Reichenbach, P.; Rossi, M. Distribution of landslides in the Upper Tiber River basin, Central Italy. *Geomorphology* **2008**, *96*, 105–122. [CrossRef]

26. Malamud, B.D.; Turcotte, D.; Guzzetti, F.; Reichenbach, P. Landslide inventories and their statistical properties. *Earth Surf. Process. Landf.* **2004**, *29*, 687–711. [CrossRef]

27. Hovius, N.; Stark, C.P.; Allen, P.A. Sediment flux from a mountain belt derived by landslide mapping. *Geology* **1997**, *25*, 231–234. [CrossRef]

28. Florsheim, J.L.; Nichols, A. Landslide area probability density function statistics to assess historical landslide magnitude and frequency in coastal California. *Catena* **2013**, *109*, 129–138. [CrossRef]

29. Fujii, Y. Frequency distribution of the magnitude of the landslide caused by heavy rainfall. *Seismol. Jpn. J.* **1969**, *22*, 244–247. [CrossRef]

30. Chen, S.C.; Chou, H.T.; Chen, S.C.; Wu, C.H.; Lin, B.S. Characteristics of Rainfall-induced Landslides in Miocene Formations: A Case Study of the Shenmu Watershed, Central Taiwan. *Eng. Geol.* **2014**, *169*, 133–146. [CrossRef]

31. Chen, C.W.; Oguchi, T.; Hayakawa, Y.S.; Saito, H.; Chen, H. Relationship between landslide size and rainfall conditions in Taiwan. *Landslides* **2016**, *14*, 1235–1240. [CrossRef]

32. Meunier, P.; Hovius, N.; Haines, J.A. Topographic site effects and the location of earthquake induced landslides. *Earth Planet. Sci. Lett.* **2008**, *275*, 221–232. [CrossRef]

33. Hejmanowska, B.; Borowiec, N.; Badurska, M. Airborne LIDAR data processing for Digital Surface Model and Digital Terrain Model generation. *Arch. Photogramm. Cartogr. Remote Sens.* **2008**, *18*, 151–162.

34. Cerovski-Darriau, C.; Roering, J.J.; Marden, M.; Palmer, A.; Bilderback, E.L. Quantifying temporal variations in landslide-driven sediment production by reconstructing paleolandscapes using tephrochronology and lidar: Waipaoa River, New Zealand. *Geochem. Geophys. Geosyst.* **2014**, *15*, 4117–4136. [CrossRef]

35. Anderson, S.; Pitlick, J. Using repeat lidar to estimate sediment transport in a steep stream. *J. Geophys. Res. Earth Surf.* **2014**, *119*, 621–643. [CrossRef]

36. Březný, M.; Pánek, T. Deep-seated landslides affecting monoclinal flysch morphostructure: Evaluation of LiDAR-derived topography of the highest range of the Czech Carpathians. *Geomorphology* **2017**, *285*, 44–57. [CrossRef]

37. Migoń, P.; Jancewicz, K.; Różycka, M.; Duszyński, F.; Kasprzak, M. Large-scale slope remodelling by landslides—Geomorphic diversity and geological controls, Kamienne Mts., Central Europe. *Geomorphology* **2017**, *289*, 134–151. [CrossRef]

38. Chan, H.C.; Chang, C.C.; Chen, S.C.; Wei, Y.S.; Wang, Z.B.; Lee, T.S. Investigation and analysis of the characteristics of shallow landslides in mountainous areas of Taiwan. *J. Chin. Soil Water Conserv.* **2015**, *46*, 19–28.

39. Gariano, S.L.; Guzzetti, F. Landlsides in a changing climate. *Earth-Sci. Rev.* **2016**, *162*, 227–252. [CrossRef]

40. Guzzetti, F.; Malamud, B.D.; Turcotte, D.L.; Reichenbach, P. Power-law correlations of landslide areas in central Italy. *Earth Planet. Sci. Lett.* **2002**, *195*, 169–183. [CrossRef]

41. Crovelli, R.A. *Probability Models for Estimation of Number and Costs of Landslides*; USGA Open-File Report 00-249; U.S. Geological Survey: Reston, VA, USA, 2000.

42. Salciarini, D.; Godt, J.W.; Baum, R.L.; Conversini, P. Modeling landslide recurrence in Seattle, Washington, USA. *Eng. Geol.* **2008**, *102*, 227–237. [CrossRef]

43. Greenhough, J.; Main, I.G. A Poisson model for earthquake frequency uncertainties in seismic hazard analysis. *Geophys. Res. Lett.* **2008**, *35*, L19313. [CrossRef]

44. Lari, S.; Frattini, P.; Crosta, G.B. A probabilistic approach for landslide hazard analysis. *Eng. Geol.* **2014**, *182*, 3–14. [CrossRef]

45. Coe, J.A.; Michael, J.A.; Crovelli, R.A.; Savage, W.Z.; Laprade, W.T.; Nashem, W.D. Probabilistic assessment of precipitation-triggered landslides using historical records of landslide Occurrence, Seattle, Washington. *Environ. Eng. Geosci.* **2004**, *10*, 103–122. [CrossRef]

46. Capital Engineering Corp. *A Study of Sediment Management Policies on Climate Change for River Basins in Southern Taiwan—GaoPing River Case Study (2/2)*; Water Resources Agency, Ministry of Economic Affairs: Taipei, Taiwan, 2011; ISBN 9789860302301.

47. Orris, G.J.; Williams, J.W. Landslide length-width ratios as an aid in landslide identification and verification. *Bull. Assoc. Eng. Geol.* **1984**, *21*, 371–375. [CrossRef]

48. Taylor, F.E.; Malamud, B.D. The statistical distributions of landslide length to width ratios. In Proceedings of the EGU General Assembly 2012, Vienna, Austria, 22–27 April 2012; Volume 14, p. 826.